Optical Materials: X 14 (2022) 100145

Contents lists available at ScienceDirect

Optical Materials: X

journal homepage: www.journals.elsevier.com/optical-materials-x

Hyperspectral microscopy of two-dimensional semiconductors

Chiara Trovatello [a,*], Armando Genco [a], Cristina Cruciano [a], Benedetto Ardini [a], Qiuyang Li [b], Xiaoyang Zhu [b], Gianluca Valentini [a], Giulio Cerullo [a,c], Cristian Manzoni [c]

[a] Dipartimento di Fisica, Politecnico di Milano, Milano, Italy
[b] Department of Chemistry, Columbia University, New York, NY, USA
[c] IFN-CNR, Milano, Italy

ARTICLE INFO

Keywords:
Transition metal dichalcogenides
Hyperspectral imaging
Photoluminescence
Strain
Machine vision

ABSTRACT

Here we present an interferometric wide field hyperspectral microscope based on a common-path birefringent interferometer with translating wedges, to measure photoluminescence emission from two-dimensional semiconductors. We show diffraction-limited hyperspectral photoluminescence microscopy from two-dimensional materials across millimeter areas, proving that our hyperspectral microscope is a compact, stable and fast tool to characterize the optical properties and the morphology of 2D materials across ultralarge areas.

1. Introduction

Optical microscopy is a powerful and non-invasive technique for the study of material properties. It can work either in point-scanning or in wide-field modalities: in the first case, the image is acquired by raster scanning over the sample a tightly focused beam and measuring the transmitted/reflected/emitted light intensity with a single detector, while in the second case a large sample area (of the order of hundreds of microns) is illuminated and imaged via a suitable optical system on a two-dimensional detector, such as a CCD. In both cases the image is typically acquired at a specific frequency, selected by a spectral filter, or integrated over a range of wavelengths, and consists of a 3D matrix in which the light intensity I is recorded as a function of the spatial coordinates (x,y).

Multispectral [1]/hyperspectral [2] microscopy is an advanced imaging technique which records a discrete/continuous spectrum of the transmitted/reflected/emitted light at each pixel of the image. Similar to single-frequency maps, the scanned regions have lateral sizes from few to hundreds of microns, depending on the objective lens used. The full collection of measured spectra at each pixel of the image generates the so-called spectral hypercube (Fig. 1a), i.e. a 3D data set consisting of the intensity as a function of two spatial coordinates (x,y) and one frequency axis (ω). From the hypercube we can either extract one image at a single frequency (Fig. 1b) or the spectrum at a single point of the image (Fig. 1c).

Multi/hyperspectral microscopes are extensively exploited in a wide range of applicative and fundamental studies, e.g. biology/medicine [3], agriculture [4], cultural heritage [5], safety [6], etc. They are usually integrated into standard wide-field microscopes and operate in the frequency domain. Typical multispectral configurations acquire a limited number of frequency channels, and they can be implemented mostly in two ways: either by placing a mosaic of a finite number of spectral filters on the detector surface [7] (Snapshot Multispectral Imaging, see Fig. 2a) or by using spectral filters [8] (either tunable, or fixed and interchangeable) in the optical path between the sample and the monochrome 2D detector (Staring Multispectral Imaging, see Fig. 2b). Hyperspectral configurations, on the other hand, measure the full spectrum at each pixel of the field of view (FOV); this is typically achieved by coupling the imaging system to a dispersive spectrometer. The hypercube is then acquired by raster scanning the sample point by point [9] (whisk-broom) or line by line [10] (push-broom, see Fig. 2c). Although these techniques are widely used, and some of them are even commercially available, the intrinsic high losses introduced by the unavoidable spectral or spatial filters impose very long acquisition times.

Both for multispectral and hyperspectral imaging the low throughput –imposed by the spectral/spatial filters- require very long acquisition times, which can be overcome by limiting the total number of measured pixels in the scanned regions. This prevents large-area materials characterization with fine spatial resolution. In the last years, compressive sensing [11] has been used to improve, after post-processing, the performances of hyperspectral imaging. Here, the FOV is photoexcited by a sequence of excitation patterns and the emission/absorption signals are

* Corresponding author.
E-mail address: chiara.trovatello@polimi.it (C. Trovatello).

https://doi.org/10.1016/j.omx.2022.100145
Received 14 January 2022; Accepted 20 February 2022
Available online 23 March 2022
2590-1478/© 2022 The Authors. Published by Elsevier B.V. This is an open access article under the CC BY license (http://creativecommons.org/licenses/by/4.0/).

acquired using a spectrometer and analyzed through an inversion algorithm. Yet, the impossibility to parallelize the acquisition of each spectrum at every pixel severely limits the acquisition time.

Here we propose an alternative high throughput and fast hyperspectral microscope, based on Fourier-transform [12] (FT) spectroscopy combined to a monochrome imaging camera. We use a birefringent interferometer, which allows to generate the phase-locked replicas of the optical waveform required for FT spectroscopy, to obtain a very compact microscopy platform [13–15]. We then apply the hyperspectral microscope to measure the emission spectra of novel two-dimensional (2D) materials and probe their optical and morphological properties across ultra-large areas (millimeter lateral size). The paper is organized as follows: Section 2 presents our innovative FT hyperspectral microscope; Section 3 reviews the properties of 2D materials; Section 4 presents results of hyperspectral imaging of 2D materials; Section 5 draws conclusions and perspectives for future work.

2. Fourier transform hyperspectral imaging

In a spectrometer based on the FT approach, the optical signal is split into two replicas, which accumulate a variable temporal delay and are then sent to a detector (see Fig. 3a). The interference between the two replicas, recorded as a function of their relative delay, gives rise to the interferogram. According to the Wiener-Khinchin theorem, the FT of the oscillating component of the interferogram yields the intensity spectrum of the optical waveform [16]. By using an array of detectors, the technique can be easily parallelized and extended to an imaging system, enabling the measurement of the spectrum for each pixel of the sample image within the FOV (Fig. 3b). In addition to the advantage offered by parallelization, FT hyperspectral imaging has other relevant advantages with respect to standard multi/hyperspectral dispersive methods. It has a higher signal to noise ratio, higher throughput (no dispersive elements are present in the detection path [17,18]) and flexible spectral resolution adjusted by setting the maximum delay of the acquired interferogram. However, one relevant requirement of the FT spectroscopy technique, which long hindered its application in the short-wavelength (short-optical cycle) visible spectral range is that the delay between the replicas must be precisely controlled at least within a small fraction (approximately 1/100) of the optical cycle (which is, e.g., 20 as for visible light with wavelength $\lambda = 600$ nm and corresponding optical cycle of 2 fs).

Previous FT hyperspectral imaging configurations were based on Michelson or Mach-Zehnder interferometers [19], which are highly sensitive to vibrations and require active stabilization or tracking with an auxiliary beam to reach the desired interferometric stability. Recently, we introduced an innovative common-path birefringent interferometer, the Translating-Wedge-based Identical pulses eNcoding System (TWINS), which has been successfully employed as a FT spectrometer with both coherent and incoherent light fields [20,21], in different photon energy ranges, i.e. from the visible to the mid-infrared. TWINS enables short acquisition times, high spatial resolution and spectral accuracy, and low background noise (−30dB).

A scheme of our hyperspectral camera is depicted in Fig. 3c. It consists of a TWINS interferometer (Pol1, B1, B2 and Pol2) followed by an imaging lens and a monochrome CMOS camera. B1 and B2 are two birefringent crystal blocks made of α-barium borate (α-BBO), while Pol1 and Pol2 are two broadband polarizers (working range 400–2000 nm) with high extinction ratio (>5000). Pol1 polarizes the input light, i.e. the PL signal, at 45° with respect to the optical axes of B1 and B2. B2 is a α-BBO plate which introduces a fixed phase delay between the two orthogonal polarizations that propagate along the fast and slow axes of the material. B1 and B2 have orthogonal optical axes, thus they introduce a delay of opposite sign between the two polarizations. B1 is shaped in the form of two wedges (see Fig. 3), and one wedge is mounted on a motorized translation stage to finely control the delay between the two replicas. The second polarizer is set at 45° with respect to the optical axes of B1 and B2 and projects the two fields back to the same polarization, ensuring interference between the two replicas. The interferometer is compact (<10 cm × 10 cm footprint), with exceptional static and dynamic delay stability in the visible spectral range. Thanks to these favorable properties, it has been successfully applied to hyperspectral imaging and microscopy. More details about the experimental setup, i.e. the camera performances, frequency calibration and resolution can be found in Ref. [14].

The parallelization capability of the interferometer enables high-quality wide-field hyperspectral microscopy, generating spectral hypercubes containing for every pixel the full spectrum.

3. Two-dimensional materials

The discovery of graphene, a one-atom-thick sheet of carbon atoms, opened up the research on other 2D materials, like semiconducting transition metal dichalcogenides (TMDs), e.g. MoS_2, $MoSe_2$, WS_2 and WSe_2. TMDs are layered semiconducting materials which comprise crystalline sheets with strong in-plane covalent bonds but weak van der Waals (vdW) out-of-plane interactions, enabling the mechanical exfoliation of individual monolayers (1L) with atomic thickness from their bulk counterpart. 1L-TMDs are at the forefront of both fundamental science and nanotechnology, including applications in photonics and optoelectronics, e.g. transistors, photodetectors, LEDs, sensors, plasmonic and tunneling devices [22]. The most interesting properties indeed arise when the system undergoes a transition from bulk/multilayer to 1L configuration, since the evolution of the band structure induces an indirect to direct bandgap transition, as evidenced by the huge

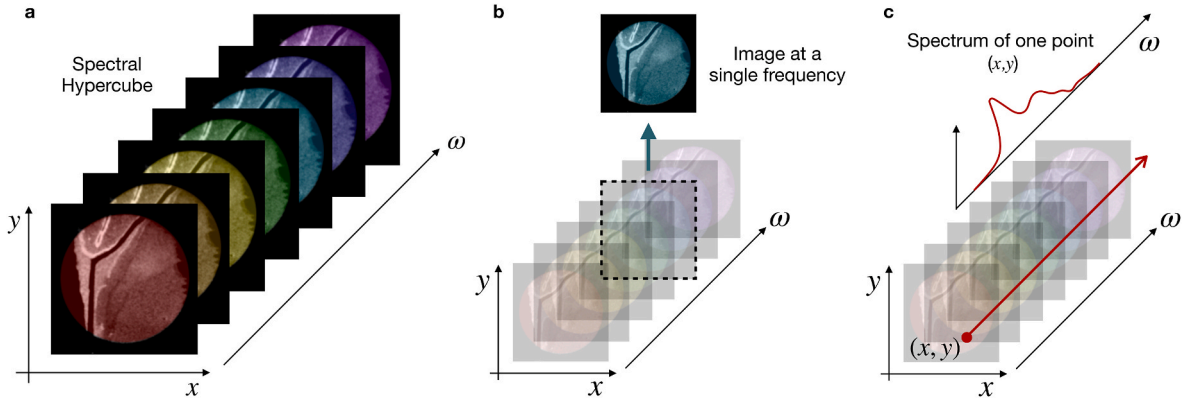

Fig. 1. Hyperspectral Imaging. (a) Hyperspectral data-cube consisting of an intensity value for each spatial coordinate *x* and *y* and frequency ω. (b) Sub-space of the hypercube consisting of one image at a single frequency. (c) Sub-space of the hypercube consisting of one spectrum at a single point (*x*,*y*).

increase of the photoluminescence (PL) quantum yield in the 1L, compared to the bilayer (2L) [23].

Excitons, i.e. bound electron-hole pairs, are the main photoexcited species in 1L-TMDs. Differently from standard 3D semiconductors, like Si or GaAs, whose exciton binding energy (E_B) is on the order of few meV, in TMDs the extreme quantum confinement and reduced Coulomb screening result in large exciton binding energies [24], up to 500 meV. The lower energy excitonic transitions, called A and B, involve electronic states at the K/K' edges of the Brillouin zone and they strongly renormalize the optical absorption spectra of 1L-TMDs [24].

Due to the weak interlayer vdW forces, TMDs can also be stacked together forming the so called vdW heterostructures [25] (HSs). Since no interlayer covalent bond is formed, the vertical stacking process can be performed without any limitation caused by the lattice mismatch between different layers. As a consequence, the physical character of each layer is preserved and the electronic/optical properties of the HS can be tailored by, e.g., the interlayer twist angle of the constituting layers. The possibility to create an innumerable quantity of new and ad-hoc tunable atomically thin materials is opening pathways for the exploration of new quantum phenomena at the nanoscale [26], like superconductivity and Moiré excitons. VdW HSs promise to revolutionize the field of photonics and optoelectronics, and also integrated linear and nonlinear optics [27].

1L-TMDs can be obtained either by mechanical exfoliation [28] from their bulk counterpart or by direct Chemical Vapor Deposition (CVD) growth [29]. CVD typically provides polycrystalline monolayers on wafer scales (cm size). Large area fabrication methods offer an alternative for a substrate-wide coverage of monolayer islands, ideally allowing for a scalable and controlled production of mono- and multilayers. This has led to a plethora of methods being developed, including top-down approaches such as liquid phase exfoliation [30] and various forms of thinning [31], as well as bottom-up routes such as wet-chemical synthesis [32], physical vapor deposition [33] and the aforementioned CVD. However, all these techniques yield polycrystalline monolayers. Moreover, large area TMDs are usually not uniform due to the challenges posed by controlling homogeneously the conditions of growth and fabrication, and they present very high defect densities and thus limited optoelectronic performances. In this context, optical characterization tools are crucial to assess the optical quality of the material on large areas in a both fast and accurate way.

On the contrary, mechanical exfoliation by the standard scotch-tape technique produces very high quality μm-sized single-crystal lattices but with very low yield, preventing massive large scale production and commercialization. The strong interest towards exfoliated samples is motivated by the fact the most of the interesting quantum phenomena can be exclusively observed in single-crystal monolayers and their related vertical stacks.

Standard mechanical exfoliation with scotch-tape typically produces a variety of flakes on a single substrate (1 cm × 1 cm), with different thickness (from 0.65 nm, monolayer, to several microns, bulk) and lateral size (from sub-micron to tens of microns) that need to be classified and selected, either for direct investigation or for stacking into vertical HSs. In the vast majority of cases, monolayers are identified by direct visual inspection under an optical microscope. The thickness characterization of the few selected "good" flakes (1–5 over hundreds) is obtained using standard optical techniques, e.g. ellipsometry, Raman and PL spectroscopy, as well as morphological characterizations, e.g. atomic force microscopy (AFM).

For instance, Raman spectroscopy can provide the number of layers in the exfoliated flake based on the energy shift of the two optical phonon modes [34], i.e. the in-plane E mode and the out-of-plane A mode. In addition, from the line shape and the intensity of the PL peak, originating from radiative emission at the optical bandgap of the material, is it possible to probe defects and disorder. An increased width of the PL peak is evidence of inhomogeneous broadening, i.e. disorder, and a reduced peak intensity identifies nonradiative recombination, which is typically mediated by defects [35].

Although such standard techniques can provide accurate thickness and quality characterization at each point of the sample, for flake search and sorting over large areas (mm-cm) this standard procedure is extremely time-consuming and labor intensive. Machine learning combined with optical spectroscopy has recently shown great potential for large area flake search [36], providing automatic search and sorting of micron-sized flakes with randomly distributed thicknesses. The different types of 2D materials can be distinguished by standard optical microscopy using color filters, i.e. tuning the RGB-based optical contrast

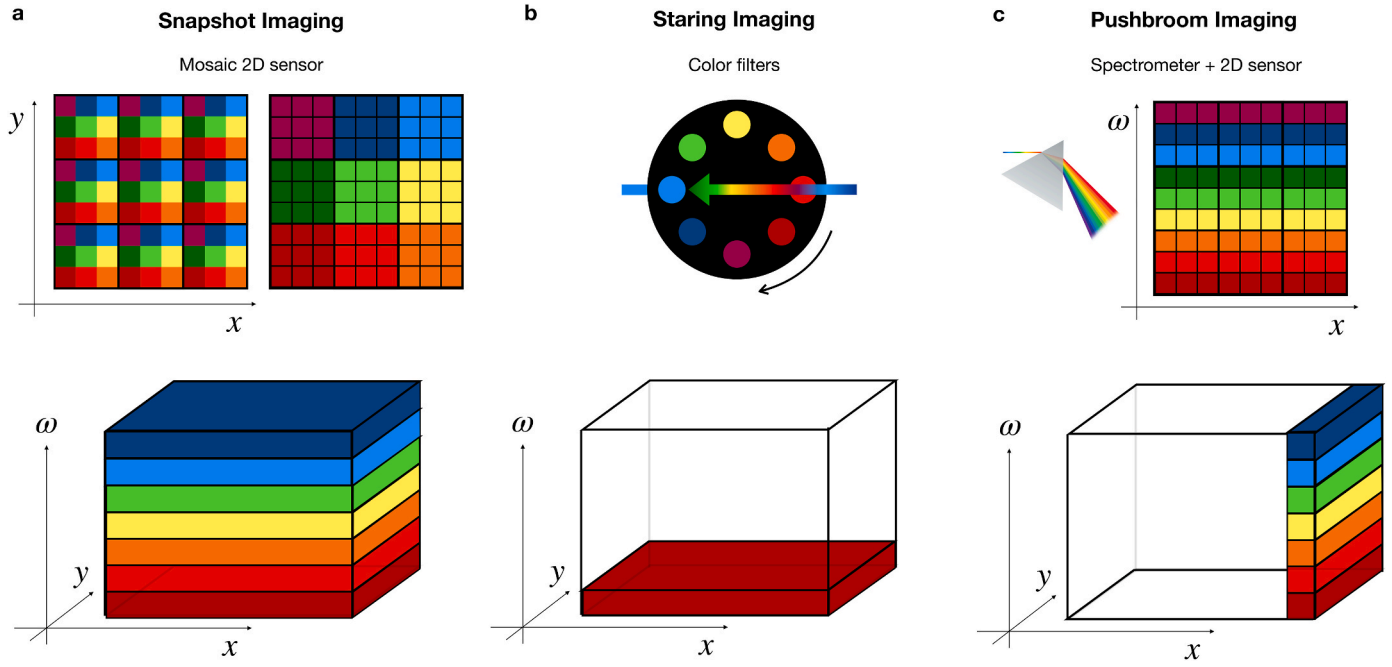

Fig. 2. Multispectral and hyperspectral imaging methods. (a) Snapshot multispectral imaging. (b) Staring multispectral imaging. (c) Push-broom hyperspectral imaging.

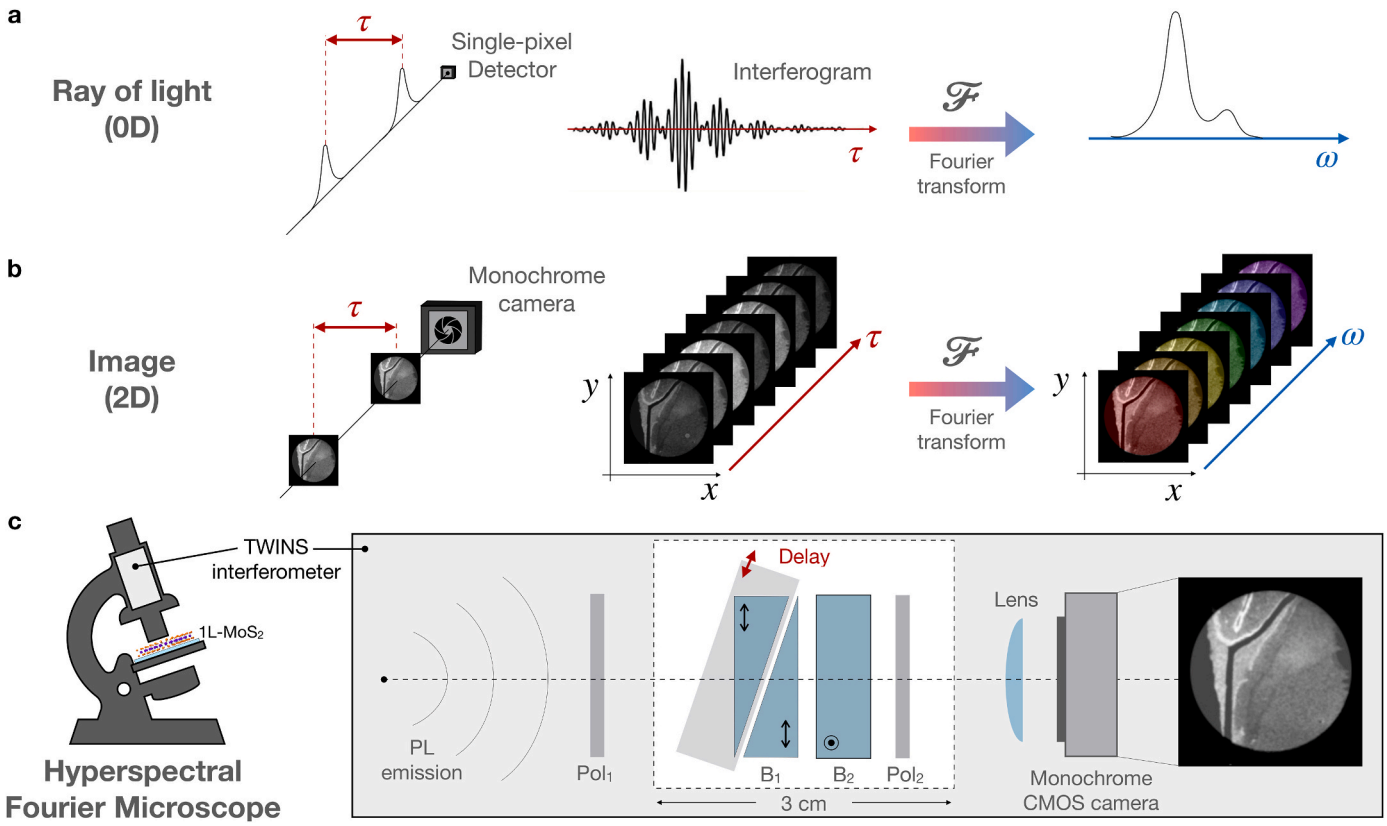

Fig. 3. Hyperspectral Fourier Microscope. (a) Working mechanism of an FT spectrometer. (b) Acquisition scheme of an hyperspectral image using an FT approach. (c) Experimental layout of our hyperspectral microscope which consists of a TWINS interferometer (Pol1, B1, B2 and Pol2) followed by a CMOS camera (monochrome imaging system). More details about the experimental setup can be found in Ref. [15].

according to their characteristic absorption. The layer thickness of the different exfoliated flakes across large areas can be estimated by complementing the optical contrast with spectroscopic techniques which are able to resolve the characteristic thickness-dependent optical spectra of the different flakes in the sample.

In addition to CVD and standard scotch tape exfoliation, a nondestructive, high-throughput technique based on a gold-assisted exfoliation has recently proven the disassembling and reassembling of 2D single-crystal monolayers with macroscopic size, limited only by the size of their bulk counterpart, with near-unity yields [37]. Although gold tape exfoliation is a deterministic process and the obtained large area monolayers possess intrinsic quality comparable to single-crystal monolayers produced by the standard scotch-tape method, their optical and electronic properties can slightly change across tens of microns sized regions in the sample. In fact, the flake cracks at multiple edges, due to the massive strain experienced during the transfer process, resulting in locally strained and doped regions on micron scales which induce strong inhomogeneity in the sample.

Single layers of TMDs are only three-atom-thick, and they have been observed to withstand large strain levels (>10%) before fracture, offering unique possibilities to engineer their electronic band structure using strain. Spatial variation of the strain in TMD layers can occur during the fabrication process, for instance during the transfer, or it can be intentionally introduced by controllable bending substrates, translating into a position-dependent bandgap modification. This leads to a spectral shift of the excitons PL intensity peak, possibly giving also rise to funneling of excitons into the areas with a larger tensile strain, where the lowest exciton energy is achieved [38,39].

Here we apply our interferometric wide field hyperspectral microscope, based on the compact and stable common-path birefringent interferometer, to measure PL spectra from exfoliated large area TMDs. We show that diffraction-limited hyperspectral PL microscopy over large areas (millimeter-sized), complemented with machine vision tools, can be used as fast technique for optical and morphological characterization of 2D crystals, i.e. identification of areas with different thickness, edges, bubbles and strained regions. The same fast and reliable method could be also applied to the classification of standard scotch tape exfoliated flakes and their selection across ultralarge areas, on a timescale of minutes.

4. Hyperspectral imaging of monolayer transition metal dichalcogenides

We use our hyperspectral microscope to measure the PL maps of gold-assisted exfoliated large area monolayer MoS_2, transferred on a reflective substrate, i.e. 90 nm-SiO_2/Si. The sample is excited by a continuous wave 532 nm laser. The laser light is delivered to the microscope by a multimode optical fiber. Subsequently, an optical system images the fiber tip to the sample plane, enabling a uniform top-hat illumination over a circular area with diameter covering 80% of the FOV. We select a 1L region with lateral size of ~600 μm × 600 μm in which tiny spurious bilayer (2L) regions are present (see Fig. 4a). We compare the monochromatic reflectance images of the sample acquired with a commercial optical microscope and two different objectives (Fig. 4a, objective 10× and Fig. 4b, objective 50×), with the corresponding PL hyperspectral images stretched in false RGB colors which represent the peak emission wavelength (Fig. 4c and d).

From the reflectance images (Fig. 4a–b), although the monolayer is cracked at multiple edges and some residual bubbles from the exfoliation process are present, the surface looks homogenous and clean over tens of microns areas. By optical contrast we can distinguish the SiO_2/Si substrate (light grey), from the 1L region (grey) and the 2L area (dark grey). On the contrary, the hyperspectral PL maps, shown in false RGB colors in Fig. 4c–d, reveal dramatic spatial variations of the PL intensity.

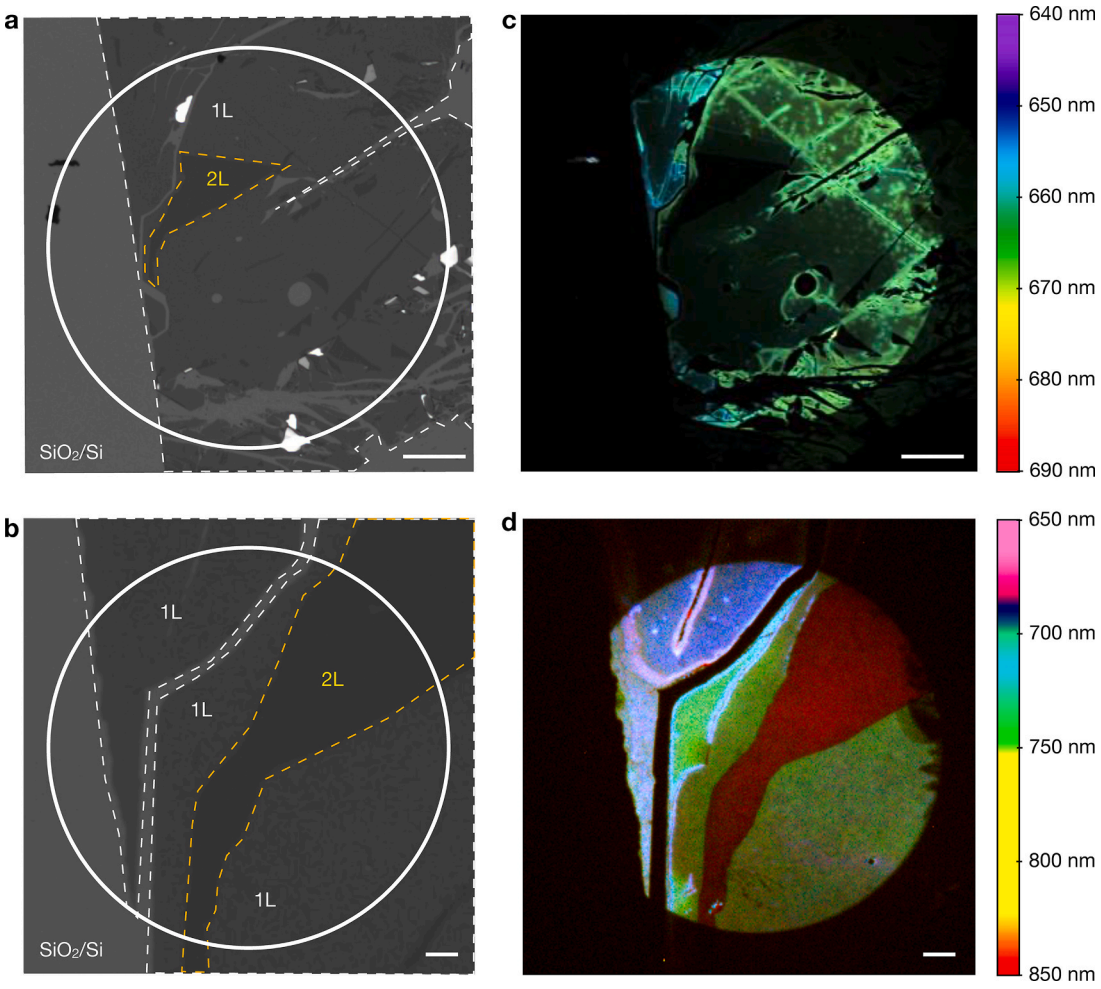

Fig. 4. Hyperspectral imaging of 1L-MoS_2. (a) Reflectance contrast image under a 10× objective, the scale bar is 100 μm. (b) Reflectance contrast image under a 50× objective, the scale bar is 10 μm. (c) Hyperspectral PL map of the sample region in panel a and (d) panel b following CW diode laser excitation at 532 nm with an average power density of 8 W/cm^2. Colorbars: false-color spectral assignment. (For interpretation of the references to color in this figure legend, the reader is referred to the Web version of this article.)

In order to quantitatively estimate the difference in the PL signals we focus on the hyperspectral map of Fig. 4d, whose integrated PL map is reported in Fig. 5a. The colored zones represent the selected 1L, 2L and substrate areas, and the corresponding spectra are shown in Fig. 5b. As expected, the bilayer displays a weaker PL intensity compared to the monolayer, due to its indirect bandgap nature. The most interesting optical emission properties come from the comparison of different spectra at different monolayer regions. In fact, Fig. 5c shows the selected 1L areas from which we extract the corresponding spectra, reported in Fig. 5d. Surprisingly the monolayer sample shows dramatically different PL spectra at different points of the sample, whose intensity changes within a factor of 4 and whose peak wavelength ranges from 656 nm to 665 nm. Such variations can result from fluctuations in dielectric environment [40], strain-induced electronic bandgap [41,42], and electrostatic potentials [43,44]. Hyperspectral imaging offers a unique tool for fast and large-area imaging of the emission properties of 2D semiconductors, providing a direct estimation of the sample inhomogeneity, which is essential for preparation optimization. We stress that, in order to obtain the same large area characterization with standard techniques, like raster-scan (whisk-broom or push-broom) PL, due to the high detection losses associated with the spectrometer, it would take at least 10 times longer (2–3 h vs. 15 min in our case) to achieve similar spatial resolution and signal to noise ratio.

In order to improve the quality of large-area TMD monolayers and to produce optically homogeneous and low-defect wafer-size devices, it is crucial to systematically characterize entire large-area samples with reliable and automatic methods (rather than employing a point-by-point manual analysis). Such hyperspectral imaging based characterization can serve as feedback to the entire preparation chain for optimization of the desired sample quality. Computer vision has been used in the field of 2D materials, predominantly as a tool for automatic mono- and multilayer identification of exfoliated material across large areas, dramatically reducing the amount of time needed for flake search. A similar approach can be also applied to hyperspectral imaging, in order to provide an innovative, compact and fast tool which is ideal for the characterization of large area fluorescent materials.

We use computer vision functions from the MATLAB Image Processing Toolbox [45] to analyze the high-resolution hyperspectral PL image of the sample. The different monolayer and bilayer TMD areas were identified via their PL, and their size and shape were extracted using MATLAB shape recognition functions. In order to measure the properties of the identified islands, it is necessary to first convert the PL image into a binary form, with pixel values set to either on (1), representing PL emission, or off (0), for areas of substrate or non-emitting thick material. This is achieved through color thresholding to isolate the different colored objects in an image. The properties of TMD islands, such as size and density, are then measured from the binary images, which mask the picture selecting only the desired areas. More details on the machine vision methods applied to large area TMD microscope images can be found in Ref. [46].

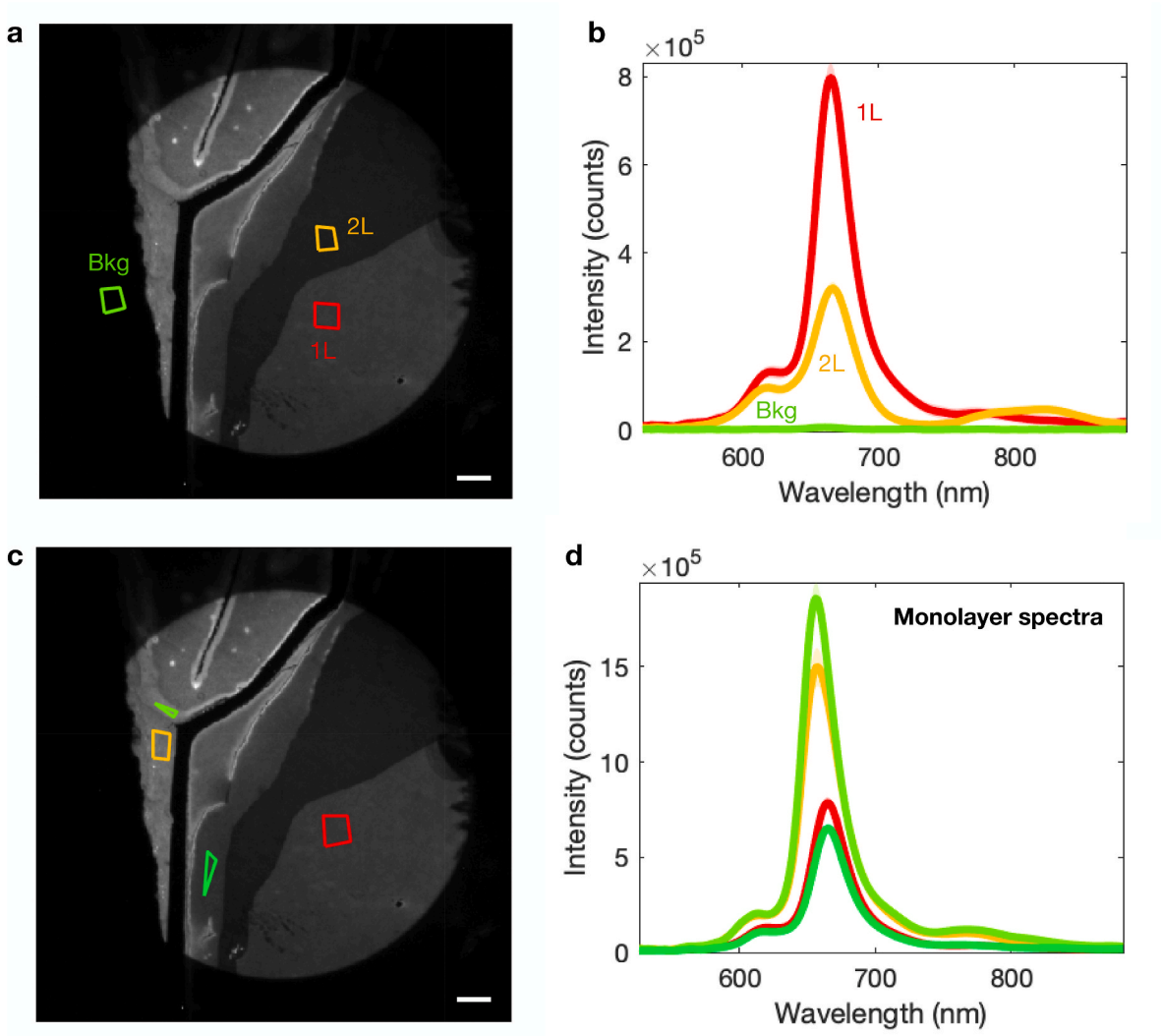

Fig. 5. Emission spectra. (a) Integrated PL intensity map. The colored zones represent the selected 1L, 2L and substrate areas. (b) Extracted spectra of the selected 1L, 2L and substrate areas. (c) Integrated PL intensity map. The colored zones here represent the different 1L regions. (d) Monolayer spectra of the selected areas. The scale bar is 10 μm.

Fig. 6 displays the results of the image processing on the stretched RGB pictures generated from the hypercubes. For the different selected color channels, the identified parts of the images are highlighted, showing in transparency the related binary image and a red square box surrounding each analyzed object. Both the 10× and 50× images from Fig. 4 have been analyzed, identifying very different areas of the sample by focusing on the color scale, being directly related to the emission spectrum of each point. By selecting shades of red, green or blue, the algorithm can easily recognize portions of the images with wrinkles, defects or areas with more uniform morphology, being also capable of clearly distinguishing and isolating the bilayer region (Fig. 6d). It is worth noticing that the combination of the high selectivity given by the color thresholding approach plus the optical contrast of stretched RGB scale generated from the high resolution hyperspectral image allow to achieve an unprecedent degree of accuracy in the identification of even very small morphological details of the analyzed samples.

Table 1 summarizes the quantitative results of the machine vision analysis, showing for each processed image the number of identified objects, the total area measured in the selected color region, the percentage of that area compared to the FOV of the hyperspectral microscope, the maximum area of a single object and the average area of the recognized islands within the sample. In this case, the machine vision analysis proved to be very useful for identifying areas with wrinkles in the image acquired with a 10× objective (Fig. 6b), or the portion of indirect bandgap bilayer present in the 50× magnification image (Fig. 6d). The capability of producing an accurate statistical analysis on the highly detailed images measured by the hyperspectral microscope makes it an ideal approach for a fast and precise characterization of large area TMD samples, in view of a large scale production.

5. Conclusion and outlook

In conclusion, we have introduced a high throughput hyperspectral microscope based on a common-path birefringent interferometer, the TWINS, to perform FT imaging on 2D materials. Our hyperspectral camera is capable of acquiring spectrally resolved fluorescence images with broad spectral coverage (300–1000 nm, i.e. 700 THz) and high spectral resolution (2.5 nm @500 nm, i.e. 3 THz), which can be easily increased upon scanning longer delays, making use of thicker birefringent wedges. By complementing our measured PL spectra with machine vision tools, we are able to rapidly assess the quality of the sample on large areas, enabling a quantitative statistical analysis of the uniformity of the fluorescent material, resolving even very small morphological details. In the future, the machine vision approach could be extended to map directly the spectral features of the samples measured by a hyperspectral microscope, such as the PL intensity or the emission peak

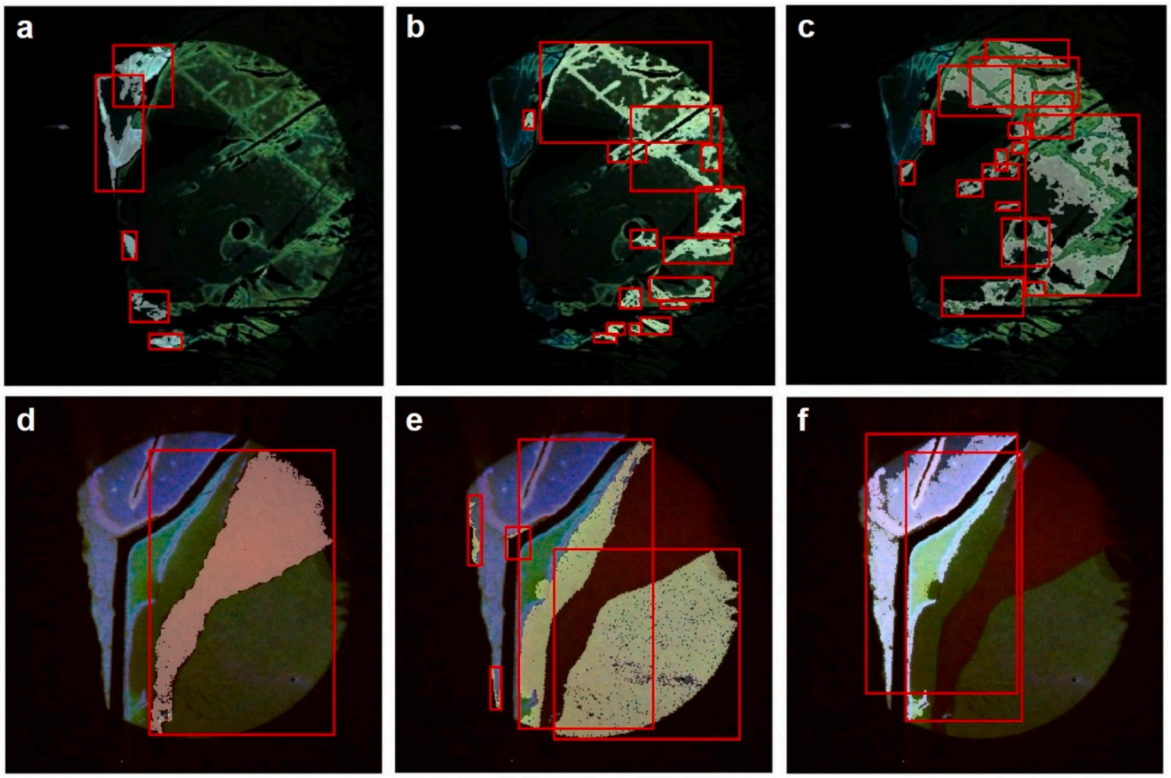

Fig. 6. Machine Vision Analysis. (a, b, c) Hyperspectral images of the sample shown in Fig. 4 in stretched RGB taken with a 10× objective processed by the machine vision algorithm. Three different color thresholds have been applied to analyze different areas of the image, highlighted in the figures. The resulting binary mask is shown in transparency together with a red box enclosing each identified object. In (d, e, f) the same procedure is applied to a hyperspectral image of the same sample taken with a 50× objective. (For interpretation of the references to color in this figure legend, the reader is referred to the Web version of this article.)

Table 1
Results of the statistical analysis on the images of Fig. 6 performed by using our machine vision tool.

Image	N. of objects analyzed	Total area (μm^2)	Partial covering (%)	Max area (μm^2)	Average area (μm^2)
6a	5	3552	4.9	1379	710
6b	15	8601	11.9	3778	573
6c	16	12644	17.5	6381	790
6d	1	399	20	399	399
6e	5	708	35.4	513	142
6f	2	366	18.3	249	183

wavelength. While our present configuration is based on silicon detectors, i.e. it can only detect light in the wavelength range 300–1000 nm, it can be straightforwardly extended to the near-infrared and mid-infrared ranges using appropriate detectors and wedges made of materials transparent in that range. We expect our hyperspectral microscope to become a powerful tool for the optical characterization of 2D crystals, semiconductors and semimetals, with optical bandgap in the visible and in the infrared, across millimetric regions and within a timescale of minutes.

Declaration of competing interest

The authors declare that they have no known competing financial interests or personal relationships that could have appeared to influence the work reported in this paper.

Acknowledgements

C.T. and G.C. acknowledge support by the European Union Horizon 2020 Programme under grant agreement no. 881603 Graphene Core 3. A.G. and G.C. acknowledge support by the European Union Marie Sklodowska-Curie Actions (project ENOSIS H2020-MSCA-IF-2020-101029644). Q. Y. and X. Z. Sample preparation at Columbia was supported by the Materials Science and Engineering Research Center (MRSEC) through NSF grant DMR-2011738.

References

[1] Jae Won Cha, Dimitrios Tzeranis, Jaichandar Subramanian, Ioannis V. Yannas, Elly Nedivi, T. Peter, C. So, Spectral-resolved multifocal multiphoton microscopy with multianode photomultiplier tubes, Opt Express 22 (2014) 21368–21381, https://doi.org/10.1364/OE.22.021368.
[2] Michael B. Sinclair, David M. Haaland, Jerilyn A. Timlin, Howland D.T. Jones, Hyperspectral confocal microscope, Appl. Opt. 45 (2006) 6283–6291, https://doi.org/10.1364/AO.45.006283.
[3] G. Lu, B. Fei, Medical hyperspectral imaging: a review, J. Biomed. Opt. 19 (1) (2014), 010901.
[4] L.M. Dale, A. Thewis, C. Boudry, I. Rotar, P. Dardenne, V. Baeten, J.A.F. Pierna, Hyperspectral imaging applications in agriculture and agro-food product quality and safety control: a review, Appl. Spectrosc. Rev. 48 (2) (2013) 142–159.
[5] C. Cucci, J.K. Delaney, M. Picollo, Reflectance hyperspectral imaging for investigation of works of art: old master paintings and illuminated manuscripts, Acc. Chem. Res. 49 (10) (2016) 2070–2079.
[6] M. Liu, T. Wang, A.K. Skidmore, X. Liu, Heavy metal-induced stress in rice crops detected using multitemporal Sentinel-2 satellite images, Sci. Total Environ. 637–638 (2018) 18–29, https://doi.org/10.1016/j.scitotenv.2018.04.415.
[7] N.A. Hagen, M.W. Kudenov, Review of snapshot spectral imaging technologies, Opt. Eng. 52 (9) (2013), 090901.
[8] N. Gat, Imaging spectroscopy using tunable filters: a review, Proc. SPIE 4056 (2000) 50–64.
[9] Peng Wang, Carl G. Ebeling, Jordan Gerton, Rajesh Menon, Hyper-spectral imaging in scanning-confocal-fluorescence microscopy using a novel broadband diffractive optic, Opt Commun. 324 (2014) 73–80, https://doi.org/10.1016/j.optcom.2014.03.044.
[10] M.E. Gehm, M.S. Kim, C. Fernandez, D.J. Brady, High-throughput, multiplexed pushbroom hyperspectral microscopy, Opt Express 16 (2008) 11032–11043.
[11] M.F. Duarte, M.A. Davenport, D. Takhar, J.N. Laska, T. Sun, K.F. Kelly, R. G. Baraniuk, IEEE Signal Process. Mag. 25 (2008) 83.

[12] S.P. Davis, M.C. Abrams, J.W. Brault, Fourier Transform Spectrometry, Elsevier, 2001.
[13] Andrew Robert Harvey, David William Fletcher-Holmes, Birefringent Fourier-transform imaging spectrometer, Opt Express 12 (2004) 5368–5374.
[14] A. Perri, B.E. Nogueira de Faria, D.C. Teles Ferreira, D. Comelli, G. Valentini, F. Preda, D. Polli, A.M. de Paula, G. Cerullo, C. Manzoni, Hyperspectral imaging with a TWINS birefringent interferometer, Opt Express 27 (2019) 15956–15967.
[15] A. Candeo, B.E. Nogueira de Faria, M. Erreni, G. Valentini, A. Bassi, A.M. de Paula, G. Cerullo, C. Manzoni, A hyperspectral microscope based on an ultrastable common-path interferometer, APL Photonics 4 (2019), 120802, https://doi.org/10.1063/1.5129860.
[16] C. Chatfield, The Analysis of Time Series—An Introduction, fourth ed., Chapman and Hall, London, 1989, pp. 94–95.
[17] P.B. Fellgett, On the ultimate sensitivity and practical performance of radiation detectors, J. Opt. Soc. Am. 39 (11) (1949) 970–976.
[18] P. Jacquinot, New developments in interference spectroscopy, Rep. Prog. Phys. 23 (1) (1960) 267–312.
[19] M.J. Persky, A review of spaceborne infrared Fourier transform spectrometers for remote sensing, Rev. Sci. Instrum. 66 (10) (1995) 4763–4797.
[20] Aurelio Oriana, Julien Réhault, Fabrizio Preda, Dario Polli, Giulio Cerullo, Scanning Fourier transform spectrometer in the visible range based on birefringent wedges, J. Opt. Soc. Am. A 33 (2016) 1415–1420.
[21] J. Réhault, R. Borrego-Varillas, A. Oriana, C. Manzoni, C.P. Hauri, J. Helbing, G. Cerullo, Fourier transform spectroscopy in the vibrational fingerprint region with a birefringent interferometer, Opt Express 25 (4) (2017) 4403–4413.
[22] T. Mueller, E. Malic, Exciton physics and device application of two-dimensional transition metal dichalcogenide semiconductors, npj 2D Mater. Appl. 2 (2018) 29, https://doi.org/10.1038/s41699-018-0074-2.
[23] Kin Fai Mak, Changgu Lee, James Hone, Jie Shan, F. Tony, Heinz. Atomically thin MoS2: a new direct-gap semiconductor, Phys. Rev. Lett. 105 (2016), 136805.
[24] Alexey Chernikov, Timothy C. Berkelbach, Heather M. Hill, Rigosi Albert, Yilei Li, Ozgur Burak Aslan, David R. Reichman, Mark S. Hybertsen, F. Tony, Heinz Phys. Rev. Lett. 113 (2014), 076802.
[25] A. Tartakovskii, Excitons in 2D heterostructures, Nat. Rev. Phys. 2 (2020) 8–9, https://doi.org/10.1038/s42254-019-0136-1.
[26] E.Y. Andrei, et al., The marvels of moiré materials, Nat. Rev. Mater. 6 (2021) 201–206.
[27] W.-T. Hsu, et al., Second harmonic generation from artificially stacked transition metal dichalcogenide twisted bilayers, ACS Nano 8 (2014) 2951–2958.
[28] K.S. Novoselov, D. Jiang, F. Schedin, T. Booth, V. Khotkevich, S. Morozov, A. K. Geim, Two-dimensional atomic crystals, Proc. Natl. Acad. Sci. Unit. States Am. 102 (2005), 1045110453.
[29] Y. Shi, H. Li, L.-J. Li, Recent advances in controlled synthesis of two-dimensional transition metal dichalcogenides via vapour deposition techniques, Chem. Soc. Rev. 44 (2015), 27442756.
[30] C. Backes, T.M. Higgins, A. Kelly, C. Boland, A. Harvey, D. Hanlon, J.N. Coleman, Guidelines for exfoliation, characterization and processing of layered materials produced by liquid exfoliation, Chem. Mater. 29 (2016) 243–255.
[31] A. Castellanos-Gomez, M. Barkelid, A. Goossens, V.E. Calado, H.S. van der Zant, G. A. Steele, Laser-thinning of MoS2: on demand generation of a single-layer semiconductor, Nano Lett. 12 (2012) 3187–3192.
[32] M. Samadi, N. Sarikhani, M. Zirak, H. Zhang, H.-L. Zhang, A.Z. Moshfegh, Group 6 transition metal dichalcogenide nanomaterials: synthesis, applications and future perspectives, Nanoscale Horiz. 3 (2018) 90–204.
[33] C. Muratore, J. Hu, B. Wang, M.A. Haque, J.E. Bultman, M.L. Jespersen, P. Shamberger, M. McConney, R. Naguy, A. Voevodin, Continuous ultra-thin MoS2 grown by low-temperature physical vapor deposition, Appl. Phys. Lett. 104 (2014), 261604.
[34] Hong Li, et al., From bulk to monolayer MoS2: evolution of Raman scattering, Adv. Funct. Mater. 22 (7) (2012) 1385–1390.
[35] Daniel Rhodes, et al., Disorder in van der Waals heterostructures of 2D materials, Nat. Mater. 18 (6) (2019) 541–549.
[36] Satoru Masubuchi, et al., Deep-learning-based image segmentation integrated with optical microscopy for automatically searching for two-dimensional materials, npj 2D Mater. Appl. 4 (1) (2020) 1–9.
[37] F. Liu, et al., Disassembling 2D van der Waals crystals into macroscopic monolayers and reassembling into artificial lattices, Science (80-.) 367 (2020) 903–906.
[38] Krishna P. Dhakal, et al., Local strain induced band gap modulation and photoluminescence enhancement of multilayer transition metal dichalcogenides, Chem. Mater. 29 (12) (2017) 5124–5133.
[39] L. Sortino, M. Brooks, P. Zotev, A. Genco, J. Cambiasso, S. Mignuzzi, S. Maier, G. Burkard, R. Sapienza, A. Tartakovskii, Dielectric nanoantennas for strain engineering in atomically thin two-dimensional semiconductors, ACS Photonics 7 (9) (2020) 2413–2422.
[40] A. Raja, L. Waldecker, J. Zipfel, Y. Cho, S. Brem, J.D. Ziegler, M. Kulig, T. Taniguchi, K. Watanabe, E. Malic, Nat. Nanotechnol. 14 (2019) 832.
[41] B.G. Shin, G.H. Han, S.J. Yun, H.M. Oh, J.J. Bae, Y.J. Song, C. Park, Y.H. Lee, Adv. Mater. 28 (2016) 9378.
[42] H. Peelaers, C.G. Van de Walle, Phys. Rev. B 86 (2012), 241401.
[43] J. Martin, N. Akerman, G. Ulbricht, T. Lohmann, J.H. v Smet, K. Von Klitzing, A. Yacoby, Nat. Phys. 4 (2008) 144.
[44] J. Xue, J. Sanchez-Yamagishi, D. Bulmash, P. Jacquod, A. Deshpande, K. Watanabe, T. Taniguchi, P. Jarillo-Herrero, B.J. Leroy, Nat. Mater. 10 (2011) 282.
[45] MathWorks, Image Processing Toolbox, User's Guide; MathWorks, 2017, pp. 195–207.
[46] T. Severs Millard, et al., Large area chemical vapour deposition grown transition metal dichalcogenide monolayers automatically characterized through photoluminescence imaging, npj 2D Mater. Appl. 4 (2020) 12.